PAPER

Check for updates

From ethene to propene (ETP) on tailored silica–alumina supports with isolated Ni(II) sites: uncovering the importance of surface nickel aluminate sites and the carbon-pool mechanism†

Zixuan Chen, [iD] [a] Scott R. Docherty, [iD] [b] Pierre Florian, [iD] [c]
Agnieszka Kierzkowska, [iD] [a] Ilia B. Moroz, [iD] [b] Paula M. Abdala, [iD] [a]
Christophe Copéret, [iD] *[b] Christoph R. Müller [iD] *[a] and Alexey Fedorov [iD] *[a]

Catalysts with well-defined isolated Ni(II) surface sites have been prepared on three silica-based supports. The outer shells of the support were comprised either of an amorphous aluminosilicate or amorphous alumina (AlO$_x$) layer – associated with a high and low density of strong Brønsted acid sites (BAS), respectively. When tested for ethene-to-propene conversion, Ni catalysts with a higher density of strong BAS demonstrate a higher initial activity and productivity to propene. On all three catalysts, the propene productivity correlates closely with the concentration of C$_8$ aromatics, suggesting that propene may form *via* a carbon-pool mechanism. While all three catalysts deactivate with time on stream, the deactivation of catalysts with Ni(II) sites on AlO$_x$, *i.e.*, containing surface Ni aluminate sites, is shown to be reversible by calcination (coke removal), in contrast to the deactivation of surface Ni silicate or aluminosilicate sites, which deactivate irreversibly by forming Ni nanoparticles.

Introduction

The development of processes for the on-purpose production of propene has been spurred in recent decades by the constantly growing demand for this important platform chemical.[1,2] Such processes include, for instance, propane dehydrogenation[3,4] or methanol-to-propene conversion.[5–7] An appealing alternative route is the direct conversion of ethene to propene, *i.e.* the ETP reaction, which to date is still underdeveloped despite its advantages (mild reaction conditions and potentially atom economy).[8] ETP catalysts based on zeolites and Al$_2$O$_3$-supported tungsten hydride have been reported.[9–11] Ni-based ETP catalysts have also been developed, such as Ni ions on mesoporous silica, *i.e.* Ni-MCM-41,[12–17] or on the Al-doped mesoporous support, Ni–Al-MCM-41.[18] The presence of Al ions induced strong Brønsted acidity of the support and was found to increase the catalytic activity.[18] Subsequently, ETP activity has been demonstrated for Ni-based catalysts on a non-mesoporous support, *i.e.*, Al-

doped silica,[19] and the formation of propene starting from ethanol has been reported as well.[20,21] Both isolated sites of Ni(II) and strong Brønsted acidity, arising from the introduction of Al, are thought to be essential for the ETP reaction to proceed.[22] Despite those advances and mechanistic insights,[23] a detailed understanding of how strong Brønsted acidity influences the catalytic performance of Ni(II) sites in the ETP reaction is still lacking.

Atomic layer deposition (ALD) is a versatile approach to prepare supports with well-controlled surface acidity properties.[24,25] Here, we utilize ALD of trimethylaluminum on partially dehydroxylated silica to prepare tailored non-mesoporous silica–alumina supports with a controlled density of strong Brønsted acid sites (BAS).[26] We then employ the surface organometallic chemistry (SOMC) approach to obtain isolated Ni(II) sites on those supports.[22,27] We prepare three catalysts, study their ETP activity and productivity to propene and correlate it to the abundance of strong Brønsted acidity, which scales from high to medium and low depending on the number of ALD cycles (1, 5 and 10, respectively).[26] A detailed product analysis identifies that along with C$_1$–C$_4$ hydrocarbons, which are typical products of the Ni-based ETP reaction, a number of aromatic products form as well, including benzene, toluene, xylenes and ethylbenzene (denoted BTXE). We find that the formation rate of propene correlates closely with the formation rate of C$_8$ aromatics, in particular xylenes. This

[a] Laboratory of Energy Science and Engineering, ETH Zürich, 8092 Zürich, Switzerland. E-mail: muelchri@ethz.ch, fedoroal@ethz.ch
[b] Department of Chemistry and Applied Biosciences, ETH Zürich, 8093 Zürich, Switzerland. E-mail: ccoperet@ethz.ch
[c] CNRS, CEMHTI UPR3079, University of Orléans, F-45071 Orléans, France

† Electronic supplementary information (ESI) available. See DOI: https://doi.org/10.1039/d2cy01272c

This journal is © The Royal Society of Chemistry 2022

Catal. Sci. Technol., 2022, **12**, 5861–5868 | **5861**

observation is consistent with the cracking of ethene oligomers, produced by the Ni(ɪɪ) sites, on cationic C_8 species (such as xylenes protonated by the strong BAS). In other words, a carbon-pool mechanism is likely responsible for the propene production on Ni-based ETP catalysts containing strong Brønsted acidity; such a pathway is reminiscent of that involved in zeolite-catalyzed ETP conversion,[28,29] and also in the methanol-to-olefins process.[30,31]

Importantly, we also uncover that the use of supports that contain an amorphous alumina (AlO_x) overlayer yields catalysts that avoid the formation of nickel nanoparticles (NPs) from isolated Ni(ɪɪ) sites with time on stream (TOS); the latter is a typical deactivation pathway of Ni-based ETP catalysts. The formation of surface nickel aluminate sites on the AlO_x overlayer is proposed to be responsible for the increased stability against deactivation by Ni NPs formation, which likely takes place by the reduction of Ni(ɪɪ) sites to metallic Ni followed by sintering. In contrast, isolated nickel silicate or aluminosilicate sites form Ni NPs with TOS and therefore do not regenerate fully during coke removal *via* calcination, while the catalysts with isolated nickel aluminate sites regenerate fully by calcination. Therefore, a combination of strong Brønsted acidity and isolated nickel aluminate sites is proposed to be essential features of active Ni-based ETP catalysts amenable to complete regeneration, while propene is proposed to form, at least in part, *via* a carbon-pool mechanism.

Results

ALD-derived silica–alumina supports with a controlled abundance of strong Brønsted acid sites were prepared using 1, 5 or 10 ALD cycles of trimethylaluminum onto silica dehydroxylated at 500 °C, as described by us previously.[26] This methodology yields supports with a high, medium and low abundance of strong Brønsted acidity. Depending on the number of cycles, the respective materials are denoted Al1-SiO$_{2\text{-}500}$, Al5-SiO$_{2\text{-}500}$ and Al10-SiO$_{2\text{-}500}$ and their surface area ranges between 280 and 160 $m^2 g^{-1}$. According to our previous detailed solid state NMR studies, the ALD-deposited shell (with a silica core) in Al1-SiO$_{2\text{-}500}$ is an amorphous aluminosilicate (ASA), which contains abundant strong BAS.[26] In contrast, Al5-SiO$_{2\text{-}500}$ and Al10-SiO$_{2\text{-}500}$ contain layers of AlO_x grown on top of the ASA shell (Fig. 1).[26] With respect to Al1-SiO$_{2\text{-}500}$, the amorphous alumina shell in Al5-SiO$_{2\text{-}500}$ features a decreased abundance of strong BAS; in Al10-SiO$_{2\text{-}500}$ the abundance of strong BAS is reduced further. Using these supports, three ETP catalysts containing isolated Ni(ɪɪ) sites were prepared by the SOMC approach.[27] This approach relies on a selective reaction between surface sites of a dehydroxylated support (such as isolated silanol or aluminol OH groups) and a molecular complex, *viz.* a grafting reaction, which in our case is a siloxide ligand exchange reaction between $[Ni(OSi(O^tBu)_3)_2]_2$ and the surface hydroxyl groups of the Al1,5,10-SiO$_{2\text{-}500}$ supports dehydroxylated at 500 °C (Fig. 1).[22] Following the grafting reaction, the materials are calcined at 400 °C (see ESI† for details) similarly to our previous report,[22] and characterized avoiding exposure to air. Henceforth, the three catalysts prepared are denoted Ni-Al1-, Ni-Al5-, Ni-Al10-SiO$_{2\text{-}500}$ and contain, according to elemental analysis, 0.73%, 1.03%, 1.09 wt% Ni, respectively.

A detailed characterization of the prepared catalysts is reported in the ESI.† In brief, the application of the
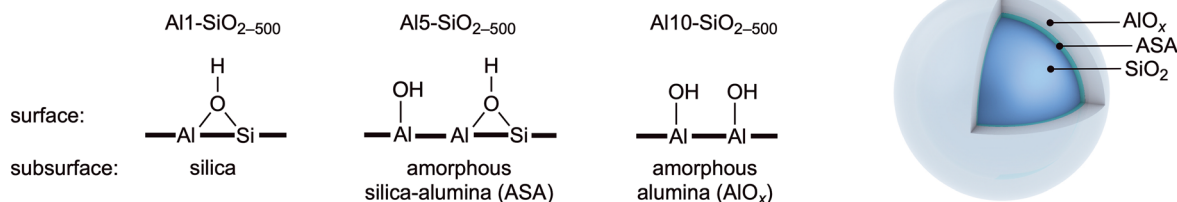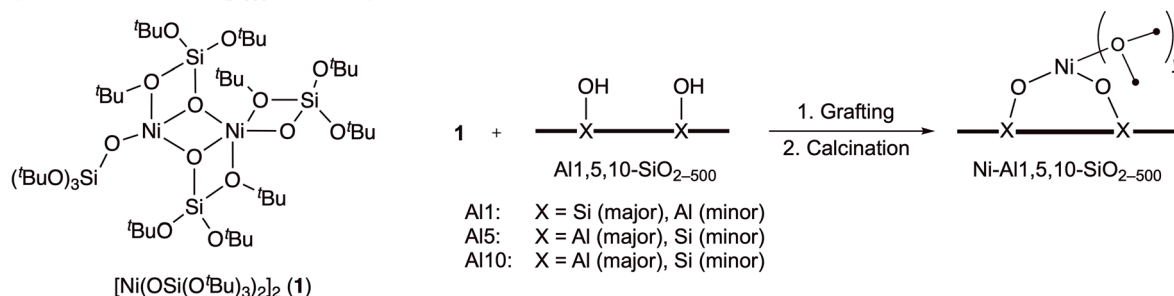
Fig. 1 The ALD-SOMC approach to yield catalysts with isolated Ni(ɪɪ) sites on the ALD-derived alumina–silica supports with a controlled density of strong Brønsted acid sites. The notations AlO_x and ASA refer to amorphous alumina and amorphous silica–alumina (an aluminosilicate layer), respectively. The structure of the calcined Ni-Al-SiO$_{2\text{-}500}$ catalysts is shown with X = Al and Si assuming a mono-grafting of $[Ni(OSi(O^tBu)_3)_2]_2$ on Al1-, Al5- and Al10-SiO$_{2\text{-}500}$ supports, and that the calcination of the mono-grafted species may, at least partially, proceed without breaking the Ni–O–Si linkage. See Table 1 for the possible range of values of variable y.

5862 | *Catal. Sci. Technol.*, 2022, **12**, 5861–5868

This journal is © The Royal Society of Chemistry 2022

combined ALD-SOMC approach yields materials that contain isolated Ni(II) sites supported on Al1,5,10-SiO$_2$-500. X-ray absorption near-edge structure (XANES) data suggests a Ni(II) oxidation state in all three catalysts (Fig. S8†). The results of the extended X-ray absorption fine structure (EXAFS) analysis of all three materials reveal the presence of Ni–O and Ni–Al(Si) coordination spheres and are indicative of the presence of isolated Ni(II) sites. The EXAFS data were fitted using Ni–O and Ni–Al/Si paths and the fitting parameters are summarized in Table 1.[32] All three Ni-Al1,5,10-SiO$_2$-500 catalysts exhibit two similar coordination spheres in EXAFS. The first coordination sphere is represented by a single Ni–O path while the second coordination sphere is fitted with two Ni–Al(Si) paths at two different interatomic distances. As discussed above, Al1-SiO$_2$-500 support is different from Al5- and Al10-SiO$_2$-500 supports in that Al1-SiO$_2$-500 has an amorphous aluminosilicate (ASA) shell while Al5- and Al10-SiO$_2$-500 supports contain an amorphous alumina (AlO$_x$) shell. Therefore, it is challenging to distinguish between Ni–Si and Ni–Al paths in Ni-Al1-SiO$_2$-500 as the atomic number of Si and Al are close.[33,34] It is likely that both Ni–Si and Ni–Al paths are present in Ni-Al1-SiO$_2$-500 while Ni–Al paths dominate the second sphere in Ni-Al5-SiO$_2$-500 and Ni-Al10-SiO$_2$-500 (Fig. S9–S11†). The presence of a Ni–Ni second coordination sphere can be ruled out (see ESI† for additional discussion), hence excluding the possibility of the formation of NiO crystallites (Tables S1 and S2, Fig. S12†). In line with the EXAFS analysis, the characteristic feature of NiO at *ca.* 8370 eV is absent in the XANES spectra of all three Ni-Al1,5,10-SiO$_2$-500 catalysts. In Ni-Al1-SiO$_2$-500, the Ni sites are likely a combination of both surface nickel silicate and nickel aluminate sites, while in Ni-Al5-SiO$_2$-500 and Ni-Al10-SiO$_2$-500 these are predominantly nickel aluminate sites.

The [27]Al nuclear magnetic resonance (NMR) spectra of Ni-Al1-, Ni-Al5-, Ni-Al10-SiO$_2$-500 display features similar to those of Al1-, Al5-, and Al10-SiO$_2$-500 reported by us previously,[26] *i.e.*, the spectra contain three overlapping peaks due to four-, five- and six-fold coordinated Al sites (Fig. S36†). The chemical shifts are found to increase with increasing number of ALD cycles, explained by more abundant Al–O–Al linkages (in preference to Al–O–Si linkages). Compared to the spectra of Al1-, Al5-, and Al10-SiO$_2$-500, there is a significant increase of

the line width in Ni-Al1-, Ni-Al5- and Ni-Al10-SiO$_2$-500 due to a larger distribution of the isotropic chemical shift values $\Delta\delta_{iso}$ (Fig. S36, Table S4†). This points at an increased chemical disorder in the Ni catalysts, likely caused by the SOMC deposition and calcination steps.

Note that a paramagnetic Ni(II) site in our catalysts "bleaches" nearby Al sites, making them invisible in the ^{27}Al NMR spectra. The normalized (with respect to the weight and the number of scans), integrated area of the NMR peaks is found to be 0.95, 4.58 and 9.77 a.u. for Ni-Al1-, Ni-Al5- and Ni-Al10-SiO$_2$-500 respectively, which corresponds to a relative ratio of 1 : 4.8 : 10.3 of aluminum atoms in the samples detected by NMR. This ratio is very close to the number of ALD cycles used (*i.e.*, 1, 5 and 10 cycles). In other words, the spatial distribution of Ni and the effect of paramagnetic bleaching is homogeneous for all three samples and no Ni clustering is evidenced by NMR, in agreement with the EXAFS data. Next, we fitted the ^{27}Al NMR spectra of Ni-Al5- and Ni-Al10-SiO$_2$-500 using the spectrum of Ni-Al1-SiO$_2$-500 as a model of the SiO$_2$–AlO$_x$ interface. The bleaching effect of Ni(II) explains the lower fitted fraction of the Ni-Al1-SiO$_2$-500 component in Ni-Al5-SiO$_2$-500 relative to Al5-SiO$_2$-500 (21% and 51%, respectively, Table S4;† the SiO$_2$–AlO$_x$ interface has been modelled in Al5-SiO$_2$-500 and Al10-SiO$_2$-500 using the spectrum of Al1-SiO$_2$-500).[26] The same effect is observed in Ni-Al10-SiO$_2$-500 relative to Al10-SiO$_2$-500 (30% and 37%, respectively), although it is notably less pronounced. Therefore, the differences in the fitting results of the Ni-Al1-SiO$_2$-500 component suggest that in Ni-Al5-SiO$_2$-500 a large fraction of the Ni(II) sites are located in the vicinity of the strong BAS of the SiO$_2$–AlO$_x$ interface, yet this is not the case in Ni-Al10-SiO$_2$-500.

FTIR studies using pyridine (Py) as the probe molecule show that bands due to the pyridinium ion (Py protonated by strong BAS) are observed clearly in Ni-Al1-SiO$_2$-500, while they are less intense in Ni-Al5-SiO$_2$-500 and nearly not discernable in Ni-Al10-SiO$_2$-500 (Fig. S13†). Those results are consistent with the degree of abundance of strong BAS in the respective Al1-, Al5- and Al10-SiO$_2$-500 supports as discussed above.[26] However, an additional Lewis acid site (LAS) emerges in Ni-Al1,5,10-SiO$_2$-500 materials, identified by an adsorbed Py band at 1614 cm^{-1} that is lacking in Al1,5,10-SiO$_2$-500 supports. This band is ascribed to Py coordinated to isolated Ni(II) sites (see ESI† for additional discussion).

Table 1 Fits of the structural parameters obtained from the Ni K-edge EXAFS data

Material	Neighbour	CN	r (Å)	σ^2 (Å^2)	E_0 (eV)	R-Factor
Ni-Al1-SiO$_2$-500	O	4.8(4)	2.00(3)	0.009(1)	−4(1)	0.002
	Si(Al)	1.5(3)	2.78(8)	0.009(1)		
	Al(Si)	2.1(4)	3.22(7)	0.009(1)		
Ni-Al5-SiO$_2$-500	O	4.9(7)	1.98(6)	0.009(1)	−8(2)	0.005
	Al(Si)	1.1(5)	2.77(9)	0.009(1)		
	Al	2.1(6)	3.19(9)	0.009(1)		
Ni-Al10-SiO$_2$-500	O	4.4(4)	1.99(4)	0.008(1)	−5(1)	0.002
	Al(Si)	1.0(3)	2.76(9)	0.008(1)		
	Al	1.7(4)	3.22(7)	0.008(1)		

All samples were measured at ambient temperature. S$_0^2$ was fixed to 0.847 obtained by fitting a Ni foil reference. CN stands for the coordination number. Debye–Waller factor σ^2 were constrained to the same value for all paths in each sample.

The catalytic performance of the prepared Ni–Al catalysts was assessed by flowing 10% C_2H_4/N_2 through a catalyst bed that was kept at 350 °C (space velocity was 200 mL g_{cat}^{-1} h^{-1}). While all three catalysts are active for ETP, their initial activity, stability with TOS and distribution of products differ significantly (Table 2). Ni-Al1-SiO$_{2-500}$, a material with the most abundant strong BAS, converts ethene notably faster than Ni-Al5-SiO$_{2-500}$ and Ni-Al10-SiO$_{2-500}$ catalysts; the respective initial (at TOS = 7 min) consumption rates of ethene are 16.8, 5.9 and 6.4 $g(C_2H_4)$ g_{Ni}^{-1} h^{-1} obtained at 55%, 20% and 30% conversion, respectively (Table 2, Fig. S14†). Interestingly, in contrast to Ni-Al1-SiO$_{2-500}$ and Ni-Al10-SiO$_{2-500}$, Ni-Al5-SiO$_{2-500}$ displays an activation period (ca. 150 min) associated with an increase of ethene conversion from ca. 20% to 25%, before deactivation sets in. Possible reasons for the activation period of Ni-Al5-SiO$_{2-500}$ are discussed below. Deactivation with TOS is observed for all three catalysts. After 20 h TOS, the conversion of Ni-Al1-, Ni-Al5- and Ni-Al10-SiO$_{2-500}$ decreases to only 8%, 10% and 3% of the initial values, respectively. The initial productivity to propene on Ni-Al1-SiO$_{2-500}$ is 2.7 $g(C_3H_6)$ g_{Ni}^{-1} h^{-1}, followed by Ni-Al10-SiO$_{2-500}$ and Ni-Al5-SiO$_{2-500}$ (0.6 and 0.2 $g(C_3H_6)$ g_{Ni}^{-1} h^{-1}, respectively). However, the productivity to propene raises after 150 min TOS for Ni-Al5-SiO$_{2-500}$ (due to an activation period mentioned above) reaching ca. 0.8 $g(C_3H_6)$ g_{Ni}^{-1} h^{-1}.

Butenes (1-butene, iso-butene, trans- and cis-2-butene) are formed on all three catalysts, consistent with the dimerization of ethene to 1-butene on the isolated Ni(II) sites followed by isomerization reactions (Fig. S16–S18†). In addition to olefins, the Ni-Al-SiO$_{2-500}$ catalysts produce C_1–C_4 alkanes, in particular ethane, whereby the partial selectivity to ethane among the C_1–C_4 alkanes exceeds 85% (Fig. S21†). The productivity to alkanes is especially high at short TOS, suggesting the formation of hydrogen (via coking) and its use for the hydrogenation of alkenes and, possibly, hydrogenolysis of alkanes. For instance, at TOS = 50 min, the productivity to C_1–C_4 alkanes is 0.79, 0.52 and 0.30 g(alkanes) g_{Ni}^{-1} h^{-1} for Ni-Al1-, Ni-Al5- and Ni-Al10-SiO$_{2-500}$, respectively (Fig. S20†). At TOS = ca. 1 h the productivity to alkanes starts to decrease for all three catalysts, before ceasing after TOS = ca. 10 h (Table 2, Fig. S16–S18†).

The initial carbon balance on Ni-Al1-, Ni-Al5-, and Ni-Al10-SiO$_{2-500}$ is only 80%, 88% and 89%, respectively. However, after 10 h on stream, all three catalysts reach ca. 100% carbon balance (Table 2, Fig. S16–S18†). The low initial carbon balance indicates the formation of non-volatile hydrocarbons and coke. Coking is also evidenced by the

change of color of the Ni-Al-SiO$_{2-500}$ catalysts from pale-grey to black after the catalytic tests and is consistent with the increase of the catalyst mass observed during in situ TGA experiments (Fig. S33†). In addition, Raman spectra of spent Ni–Al catalysts reveal two main peaks centered at ca. 1350 cm^{-1} and 1580 cm^{-1}, ascribed to the disordered carbon and ordered graphitic lattice, respectively (Fig. S32†).[35] The ratio between these peaks, i.e., the D_1/G area ratio, is used to evaluate the degree of disorder in the graphitic coke deposits. While similar D_1/G ratio of 1.5 was obtained for Ni-Al1-SiO$_{2-500}$ and Ni-Al5-SiO$_{2-500}$, Ni-Al10-SiO$_{2-500}$ features a lower D_1/G ratio of 0.3 (see ESI† for further details). The evolution of the productivity to alkanes with TOS correlates closely with that of coking (evaluated by the carbon balance) and the formation of H_2 (Fig. S20†).

Interestingly, aromatic products (benzene, toluene, xylenes, ethylbenzene, BTXE) form on all three Ni-Al-SiO$_{2-500}$ catalysts. Ni-Al1-SiO$_{2-500}$ exhibits the highest productivities to toluene and C_8 aromatics (ethylbenzene and o-, m-, p-xylene) whereas Ni-Al10-SiO$_{2-500}$ produces predominantly benzene at TOS = 7 min (Fig. S19†).[36] After TOS = 8 h, the partial selectivity (i.e., the selectivity among aromatic products) to C_8 aromatics is more than 60% on all three catalysts. Control experiments show that the respective supports Al1-, Al5-, and Al10-SiO$_{2-500}$ do not catalyze ETP, nor do they form any aromatic products (Fig. S30†). The initial ethene conversion on these supports does not exceed 5% and is likely due to the formation of coke.

To understand the nature of the surface species formed during the ETP experiment, Ni-Al5-SiO$_{2-500}$ was heated with a 1:1 mixture of $^{13}C_2H_4/C_2H_4$ at 350 °C for 12 h. The subsequently acquired ^{13}C CP-MAS spectrum of the resulted black solid shows two major peaks in the range 110–150 ppm and 10–40 ppm, assigned to aromatic carbonaceous species and aliphatic groups, respectively (Fig. S38†). The presence of such species has been ascribed previously to the formation of alkylated aromatic hydrocarbons in zeolites,[37–39] and in other alumina-based catalysts.[40] Furthermore, comparing the ^1H spin-echo spectra of Ni-Al5-SiO$_{2-500}$ after exposure to $^{13}C_2H_4/$ C_2H_4 (350 °C, 12 h) with that of fresh Ni-Al5-SiO$_{2-500}$, confirms the emergence of peaks at ca. 2 ppm and 7 ppm, consistent with benzylic and aromatic protons, respectively (Fig. S39†); the peak at ca. 21 ppm in ^{13}C NMR spectrum further suggests the presence of Ar–CH_3 benzylic groups (Fig. S38†). Notably, no additional signals are observed in the range 4–6 ppm, ruling out the presence of adsorbed olefinic species (i.e. ethene, propene, butenes, etc.). Analysis of the gas phase of

Table 2 Results of ICP analysis and catalytic tests. Catalytic data is presented after 7 min TOS and, in parentheses, after 20 h TOS

Entry	Catalyst	Ni content (wt%)	Ethene conversion (%)	Propene productivity (g g_{Ni}^{-1} h^{-1})	C_4 olefins productivity (g g_{Ni}^{-1} h^{-1})	C_1–C_4 alkane productivity (g g_{Ni}^{-1} h^{-1})	H_2 productivity (g g_{Ni}^{-1} h^{-1})	Carbon balance (%)
1	Ni-Al1-SiO$_{2-500}$	0.73	55 (8)	2.7 (0.6)	5.5 (1.8)	1.1 (0.1)	0.16 (0.005)	80 (100)
2	Ni-Al5-SiO$_{2-500}$	1.03	20 (10)	0.2 (0.5)	0.3 (1.3)	0.2 (0.1)	0.03 (0.003)	88 (100)
3	Ni-Al10-SiO$_{2-500}$	1.09	30 (3)	0.6 (0.1)	1.7 (0.4)	0.4 (0.1)	0.02 (0.004)	89 (100)

the batch experiment by GC-MS confirms the formation of a statistical mixture of ^{13}C isotopologues of propene (Fig. S41, Table S6†). In addition to propene, ethane is detected and its formation is explained by the hydrogenation of ethene by H_2 (formed due to coking) over the course of the experiment. However, in contrast to propene, ethane features mostly a mixture of unlabelled and di-labelled isotopologues with only a small amount (ca. 5%) of the mono-labelled isotopologue (Fig. S40, Table S5†). This result is inconsistent with the presence of olefin metathesis based ETP mechanism that has been proposed previously for Ni-based catalysts,[12] and is in line with the cracking pathways.[23]

Transmission electron microscopy (TEM) imaging and energy dispersive X-ray (EDX) mapping of spent Ni-Al1-SiO$_{2-500}$ (i.e., after 20 h TOS) reveal the formation of Ni NPs (Fig. S22†). This is explained by the evolution of Ni(II) sites to reduced Ni species under reaction conditions, their de-grafting (dissociation) from the support and agglomeration to Ni NPs (either metallic Ni, carburized Ni, or a mixture of thereof). Note that no Ni NPs are observed in any of the fresh catalysts (Fig. S4–S6†). Interestingly, in contrast to Ni-Al1-SiO$_{2-500}$, no Ni NPs are found in spent Ni-Al5-SiO$_{2-500}$ and Ni-Al10-SiO$_{2-500}$; EDX mappings show that the Ni sites remain homogenously distributed on Ni-Al5-SiO$_{2-500}$ and Ni-Al10-SiO$_{2-500}$ after the 20 h catalytic test (Fig. S23 and S24†). Our observations, i.e. the formation of coke and the retention of isolated Ni sites on deactivated Ni-Al5-SiO$_{2-500}$ and Ni-Al10-SiO$_{2-500}$ catalysts, suggest that regeneration of the initial activity by calcination should be viable for these two catalysts.

To test this hypothesis, the reaction–regeneration cycles were carried out by passing synthetic air at 500 °C for 1 h (to remove coke) through the catalyst bed that has been exposed for 5 h to ETP conditions. No substantial changes in the productivity of propene (except for the increased propene productivity after the first regeneration cycle for Ni-Al5-SiO$_{2-500}$, vide infra) were observed between the first, second and indeed up to the fifth regeneration cycle for Ni-Al5-SiO$_{2-500}$ and Ni-Al10-SiO$_{2-500}$, suggesting that these catalysts can be fully regenerated (Fig. 2). However, regeneration of Ni-Al1-SiO$_{2-500}$ could restore the propene productivity of the previous cycles only partially. Those observations further confirm the differences in the deactivation mechanisms between Ni-Al1-SiO$_{2-500}$ on one hand and Ni-Al5- and Ni-Al10-SiO$_{2-500}$ on the other hand, consistent with the TEM results. In other words, two deactivation pathways proceed in Ni-Al1-SiO$_{2-500}$ during ETP, i.e. (i) the formation of Ni NPs due to the reduction of
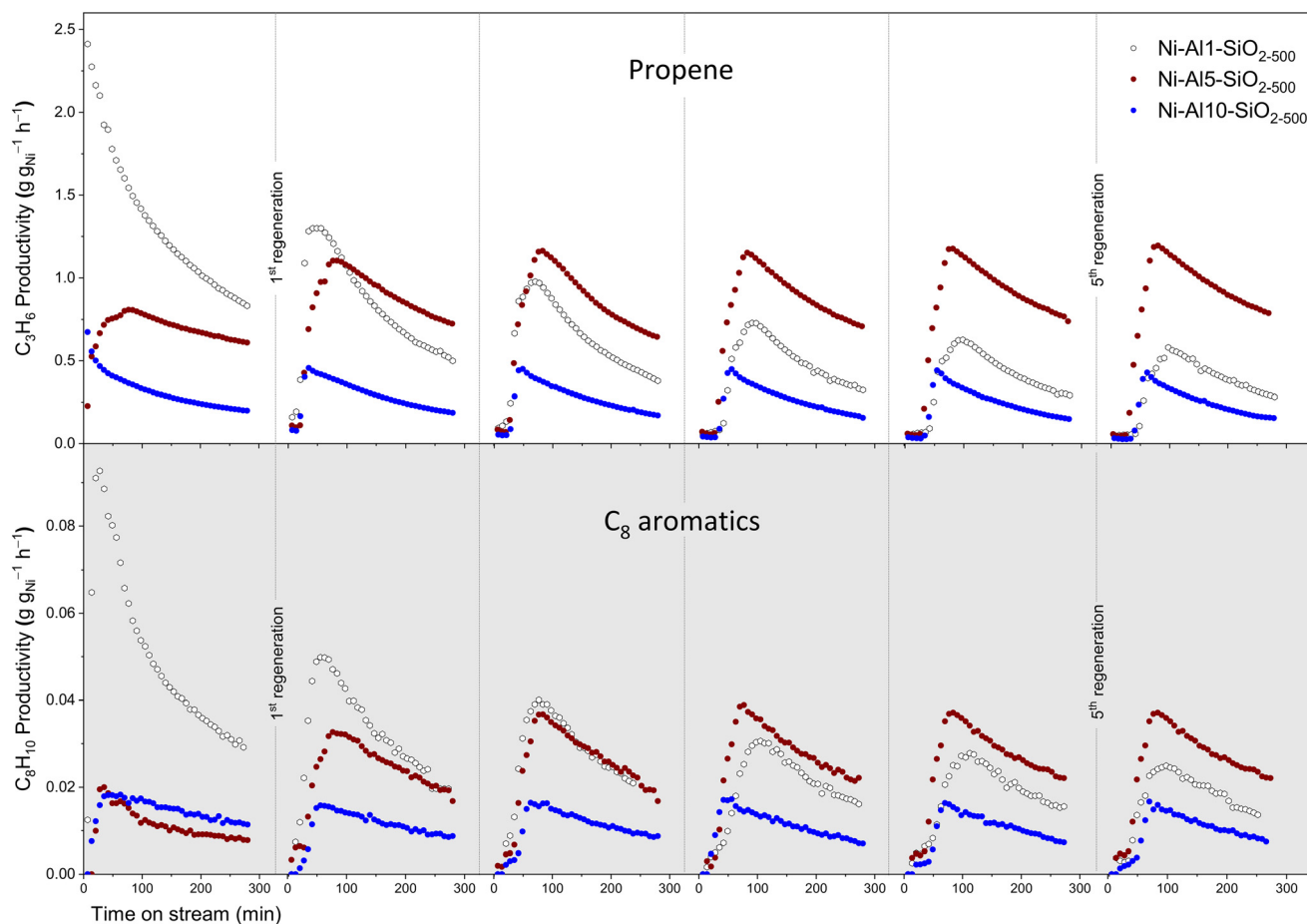

Fig. 2 The productivity to propene and C_8 aromatics (ethylbenzene and o-, m-, p-xylene) on Ni-Al1-, Ni-Al5- and Ni-Al10-SiO$_{2-500}$ catalysts (black-and-white, red and blue symbols, respectively) over in total 30 h TOS including five regeneration cycles (after every 5 h TOS).

This journal is © The Royal Society of Chemistry 2022

Catal. Sci. Technol., 2022, 12, 5861–5868 | 5865

Ni(II) single sites and the agglomeration of the reduced species (see above, Fig. S22†) and (ii) coke deposition. While coke can be removed by calcination, the oxidation of the agglomerated Ni NPs gives NiO, which, in contrast to isolated sites of Ni(II), does not catalyze the oligomerization of ethene efficiently. In contrast, the Ni-Al5- and Ni-Al10-SiO$_{2-500}$ catalysts deactivate only by coke deposition (*i.e.*, blocking of the active sites by coke) since their catalytic activity is fully recovered after regeneration by calcination.
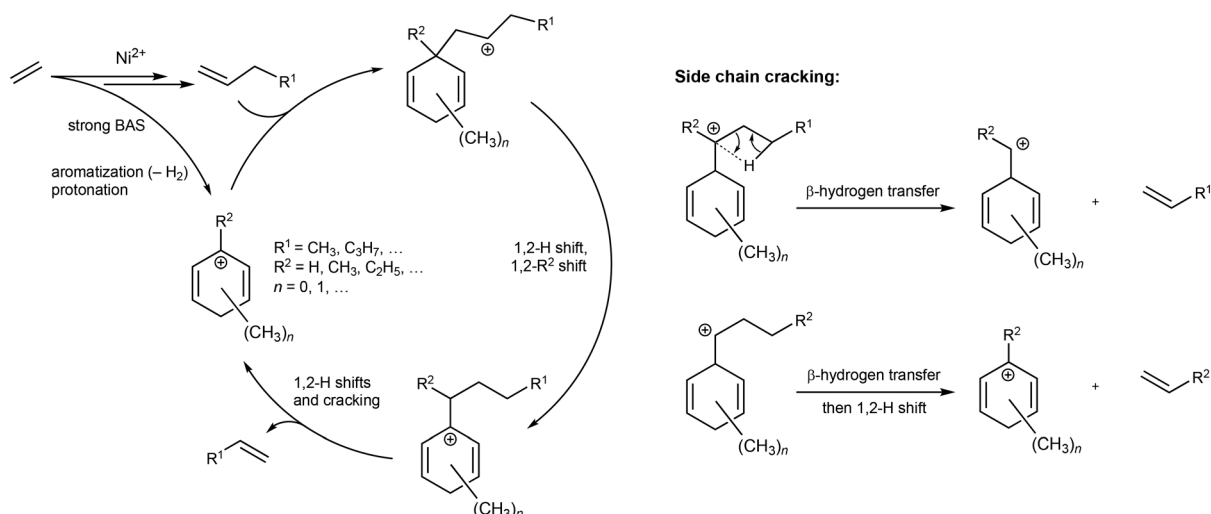
Interestingly, after the first regeneration cycle, Ni-Al5-SiO$_{2-500}$ displays a propene productivity that is increased by *ca.* 30% and which is maintained in every subsequent ETP-regeneration cycle (Fig. 2). We note that the temperature used for regeneration is higher relative to the initial calcination temperature of the grafted Ni species (500 °C and 400 °C, respectively). This higher temperature is required because coke removal is incomplete at 400 °C, and as a result, a longer activation period and a lower maximum propene productivity is observed if a regeneration temperature of 400 °C is used instead of a regeneration temperature of 500 °C (Fig. S34†). However, if Ni-Al5-SiO$_{2-500}$ is prepared by calcination of the grafted Ni species at 500 °C, the resulted propene productivities of the fresh and the regenerated catalysts are similar (Fig. S31†). Therefore, the observed increase by *ca.* 30% in the propene productivity of Ni-Al5-SiO$_{2-500}$ may be due to a structural evolution of Ni-Al5-SiO$_{2-500}$ at 500 °C.

To probe for possible structural changes of Ni-Al5-SiO$_{2-500}$ during the regeneration process, we have applied ^{27}Al MAS NMR spectroscopy. The narrower spectral lines in Ni-Al5-SiO$_{2-500-regen}$ reveal a higher structural ordering in this material, yet the lines become also narrower in the Ni-free reference Al5-SiO$_{2-500-regen}$ (Fig. S37†). In addition, the relative fractions of ^{4}Al/^{5}Al/^{6}Al sites change in both Ni-Al5-SiO$_{2-500-regen}$ and Al5-SiO$_{2-500-regen}$ (Table S4†). The modelling of Ni-Al5-SiO$_{2-500-regen}$ shows smaller $\Delta\delta_{iso}$ and $\bar{C}_Q$ than in fresh Ni-Al5-SiO$_{2-500}$ (both modellings use three Al sites). In addition, a shift of $\bar{\delta}_{iso}$ towards higher chemical shifts and a decreased proportion of four-coordinated aluminum environments is observed after regeneration. This points to a complex mechanism for the structural reorganization during regeneration involving not only the OH groups (usually at the origin of the coordination increase), but also the chemical Al/Si mixing, which drives changes in $\bar{\delta}_{iso}$.[26] Differences in the NMR parameters of Al5-SiO$_{2-500-regen}$ and Ni-Al5-SiO$_{2-500-regen}$ show that Ni also plays a role in the structural ordering of the catalysts during regeneration.

The activation time that lasts *ca.* 50–100 min is observed in all Ni-Al-SiO$_{2-500}$ catalysts following regeneration; in addition, fresh Ni-Al5-SiO$_{2-500}$ features an activation period as well. After 90 min TOS, following the sixth regeneration, *i.e.* close to the highest propene productivity, the three Ni–Al catalysts were collected and FTIR spectra were recorded without exposure to air. The spectra of fresh and regenerated catalysts after 90 min TOS are similar (Fig. S25†). That being said, the comparison between the Py-FTIR spectra of fresh and regenerated Ni-Al5-SiO$_{2-500}$ catalysts reveals a decreased relative intensity of the IR band corresponding to the Lewis acidic Ni(II) sites as compared to the intensity of Py on the Al-based LAS on the regenerated catalysts (Fig. S35†). This result suggests that restructuring of the catalyst surface after calcination may occur with TOS, although more studies are needed to understand details of this process. Lastly, TEM images and EDX mapping of the activated and spent Ni-Al-SiO$_{2-500}$ catalysts are also similar, *i.e.* Ni NPs are only observed in activated and spent Ni-Al1-SiO$_{2-500}$ and not observed in Ni-Al5-SiO$_{2-500}$ and Ni-Al10-SiO$_{2-500}$ (Fig. S27–S29†).

Interestingly, comparing changes in the productivity to aromatic products with TOS, in particular C$_8$ aromatics, with changes in the productivity to propene reveal a very clear correlation (Fig. 2 and S15†). For instance, the continuously decreasing propene productivity on Ni-Al1-SiO$_{2-500}$ with every additional regeneration cycle correlates closely with the decreasing productivity to C$_8$ aromatics. This result suggests that the formation of propene may involve the intermediacy of alkylated aromatics (and, possibly, *vice versa*). The results

Scheme 1 A possible propene formation pathway involving the carbon-pool mechanism.

5866 | *Catal. Sci. Technol.*, 2022, **12**, 5861–5868

This journal is © The Royal Society of Chemistry 2022

discussed above are consistent with the following reaction mechanism. Ethene is first dimerized to 1-butene and then oligomerized further on Ni(II) sites,[41] whereas strong BAS catalyze olefin aromatization to BTXE,[42] and provide protonated aromatic species that can be alkylated by olefins such as 1-butene. Cracking of the side chain of the resulting intermediates may form propene and regenerate the cationic aromatic species (Scheme 1). This carbon-pool mechanism is thus complementary to the ETP mechanisms proposed previously (chain growth on Ni sites and cracking of oligomers on the strong BAS),[22] and is related to the pathways of the zeolite-catalyzed ETP reaction.[28,29]

In conclusion, we have reported that Ni-based catalysts with abundant strong BAS show a higher propene productivity relative to catalysts with less abundant strong BAS. The role of the strong BAS is not only limited to the cracking of ethene oligomers, but they also catalyze the aromatization of ethene and higher olefins to BTXE products. When protonated, these aromatics can be further alkylated, which in turn facilitates the cracking process (*i.e.*, the carbon-pool mechanism). Lastly, the formation of Ni aluminate sites on the amorphous alumina overlayer prevents Ni(II) from overreduction which would lead to the formation of Ni nanoparticles. These findings expand the scope and understanding of Ni-based catalysts in the ETP reaction. Our future work will focus on the development of isolated Ni(II) sites that are stable under ETP conditions in the presence of abundant strong BAS. Moreover, kinetic studies will be needed to improve our understanding of the role of the cracking of linear oligomers *vs.* the cracking of alkylated aromatic species in the ETP reaction.

Conflicts of interest

There are no conflicts to declare.

Acknowledgements

References

1 J. S. Plotkin, *Catal. Today*, 2005, **106**, 10–14.

2 H. A. Wittcoff, B. G. Reuben and J. S. Plotkin, *Industrial Organic Chemicals*, John Wiley & Sons, Inc., Hoboken, New Jersey, 2nd edn, 2004.

3 S. R. Docherty, L. Rochlitz, P. A. Payard and C. Copéret, *Chem. Soc. Rev.*, 2021, **50**, 5806–5822.

4 S. Chen, X. Chang, G. Sun, T. Zhang, Y. Xu, Y. Wang, C. Pei and J. Gong, *Chem. Soc. Rev.*, 2021, **50**, 3315–3354.

5 A. Galadima and O. Muraza, *Ind. Eng. Chem. Res.*, 2015, **54**, 4891–4905.

6 U. Olsbye, M. Bjørgen, S. Svelle, K.-P. Lillerud and S. Kolboe, *Catal. Today*, 2005, **106**, 108–111.

7 M. A. Ali, S. Ahmed, N. Al-Baghli, Z. Malaibari, A. Abutaleb and A. Yousef, *Catal. Lett.*, 2019, **149**, 3395–3424.

8 C. Copéret, F. Allouche, K. W. Chan, M. P. Conley, M. F. Delley, A. Fedorov, I. B. Moroz, V. Mougel, M. Pucino, K. Searles, K. Yamamoto and P. A. Zhizhko, *Angew. Chem., Int. Ed.*, 2018, **57**, 6398–6440.

9 B. Lin, Q. Zhang and Y. Wang, *Ind. Eng. Chem. Res.*, 2009, **48**, 10788–10795.

10 M. Taoufik, E. Le Roux, J. Thivolle-Cazat and J. M. Basset, *Angew. Chem., Int. Ed.*, 2007, **46**, 7202–7205.

11 E. Mazoyer, K. C. Szeto, N. Merle, J. Thivolle-Cazat, O. Boyron, J.-M. Basset, C. P. Nicholas and M. Taoufik, *J. Mol. Catal.*, 2014, **385**, 125–132.

12 M. Iwamoto and Y. Kosugi, *J. Phys. Chem. C*, 2007, **111**, 13–15.

13 K. Ikeda, Y. Kawamura, T. Yamamoto and M. Iwamoto, *Catal. Commun.*, 2008, **9**, 106–110.

14 T. Lehmann, T. Wolff, V. M. Zahn, P. Veit, C. Hamel and A. Seidel-Morgenstern, *Catal. Commun.*, 2011, **12**, 368–374.

15 A. S. Frey and O. Hinrichsen, *Microporous Mesoporous Mater.*, 2012, **164**, 164–171.

16 M. Tanaka, A. Itadani, Y. Kuroda and M. Iwamoto, *J. Phys. Chem. C*, 2012, **116**, 5664–5672.

17 T. Lehmann, T. Wolff, C. Hamel, P. Veit, B. Garke and A. Seidel-Morgenstern, *Microporous Mesoporous Mater.*, 2012, **151**, 113–125.

18 L. Alvarado Perea, T. Wolff, P. Veit, L. Hilfert, F. T. Edelmann, C. Hamel and A. Seidel-Morgenstern, *J. Catal.*, 2013, **305**, 154–168.

19 M. Stoyanova, M. Schneider, M.-M. Pohl and U. Rodemerck, *Catal. Commun.*, 2017, **92**, 65–69.

20 M. Iwamoto, K. Kasai and T. Haishi, *ChemSusChem*, 2011, **4**, 1055–1058.

21 M. Iwamoto, *Molecules*, 2011, **16**, 7844–7863.

22 I. B. Moroz, A. Lund, M. Kaushik, L. Severy, D. Gajan, A. Fedorov, A. Lesage and C. Copéret, *ACS Catal.*, 2019, **9**, 7476–7485.

23 U. Rodemerck, E. V. Kondratenko, M. Stoyanova and D. Linke, *J. Catal.*, 2020, **389**, 317–327.

24 A. R. Mouat, C. George, T. Kobayashi, M. Pruski, R. P. van Duyne, T. J. Marks and P. C. Stair, *Angew. Chem., Int. Ed.*, 2015, **54**, 13346–13351.

25 A. G. M. Rankin, P. B. Webb, D. M. Dawson, J. Viger-Gravel, B. J. Walder, L. Emsley and S. E. Ashbrook, *J. Phys. Chem. C*, 2017, **121**, 22977–22984.

26 M. Kaushik, C. Leroy, Z. Chen, D. Gajan, E. Willinger, C. R. Müller, F. Fayon, D. Massiot, A. Fedorov, C. Copéret, A. Lesage and P. Florian, *Chem. Mater.*, 2021, **33**, 3335–3348.

27 C. Coperet, A. Comas-Vives, M. P. Conley, D. P. Estes, A. Fedorov, V. Mougel, H. Nagae, F. Nunez-Zarur and P. A. Zhizhko, *Chem. Rev.*, 2016, **116**, 323–421.

28 K. Lee and S. B. Hong, *ACS Catal.*, 2019, **9**, 10640–10648.

29 W. Dai, X. Sun, B. Tang, G. Wu, L. Li, N. Guan and M. Hunger, *J. Catal.*, 2014, **314**, 10–20.

30 P. Tian, Y. Wei, M. Ye and Z. Liu, *ACS Catal.*, 2015, **5**, 1922–1938.

31 S. Ilias and A. Bhan, *ACS Catal.*, 2012, **3**, 18–31.

32 K. Horioka, K. Takahashi, N. Morimoto, H. Horiuchi, M. Akaogi and S. Akimoto, *Acta Crystallogr., Sect. B: Struct. Crystallogr. Cryst. Chem.*, 1981, **37**, 635–638.

33 B. K. Teo, *EXAFS: Basic Principles and Data Analysis*, Springer-Verlag, Berlin, Heidelberg, New York, Tokyo, 1986.

34 J. Timoshenko and A. Kuzmin, *Comput. Phys. Commun.*, 2009, **180**, 920–925.

35 A. Sadezky, H. Muckenhuber, H. Grothe, R. Niessner and U. Pöschl, *Carbon*, 2005, **43**, 1731–1742.

36 C. Wang, X. Zhao, M. Hu, G. Qi, Q. Wang, S. Li, J. Xu and F. Deng, *Angew. Chem., Int. Ed.*, 2021, **60**, 23630–23634.

37 P. Ferri, C. Li, C. Paris, A. Vidal-Moya, M. Moliner, M. Boronat and A. Corma, *ACS Catal.*, 2019, **9**, 11542–11551.

38 J. T. C. Wennmacher, S. Mahmoudi, P. Rzepka, S. Sik Lee, T. Gruene, V. Paunovic and J. A. van Bokhoven, *Angew. Chem., Int. Ed.*, 2022, **61**, e202205413.

39 J. P. Lange, A. Gutsze, J. Allgeier and H. G. Karge, *Appl. Catal.*, 1988, **45**, 345–356.

40 M. A. Callejas, M. T. Martínez, T. Blasco and E. Sastre, *Appl. Catal., A*, 2001, **218**, 181–188.

41 E. Koninckx, P. S. F. Mendes, J. W. Thybaut and L. J. Broadbelt, *Appl. Catal., A*, 2021, **624**, 118296.

42 E. A. Uslamin, H. Saito, N. Kosinov, E. Pidko, Y. Sekine and E. J. M. Hensen, *Catal. Sci. Technol.*, 2020, **10**, 2774–2785.

5868 | *Catal. Sci. Technol.*, 2022, **12**, 5861–5868

This journal is © The Royal Society of Chemistry 2022